ENGINEERING Environment
2026, 20(5): 67 https://doi.org/10.1007/s11783-026-2167-z

RESEARCH ARTICLE

Enhanced rare earth element recovery from NdFeB leachates using magnetically responsive vermiculite–alginate nanocomposites

Giani de Vargas Brião[1], Cláudia Batista Lopes ✉ [2], Ana Cristina Estrada[2], Tito Trindade[2], Carlos Manuel Silva[2,3], Meuris Gurgel Carlos da Silva[1], Melissa Gurgel Adeodato Vieira ✉ [1]

1. School of Chemical Engineering, University of Campinas, Campinas 13083-852, Brazil
2. Department of Chemistry, CICECO-Aveiro Institute of Materials, University of Aveiro, Aveiro 3810-193, Portugal
3. CERES- Department of Chemical Engineering, University of Coimbra, Faculty of Sciences and Technology, Coimbra 3030-790, Portugal

HIGHLIGHTS

- Vermiculite was well integrated in the synthesis of magnetic nanoparticles (MNPs).
- Fe_3O_4@vermiculite MNPs encapsulated in alginate beads enabled magnetic separation.
- Nd(III) was effectively recovered from an NdFeB magnets leachate.
- DTPA and EDTA were highly effective in recovering sorbed Rare Earth Metals.

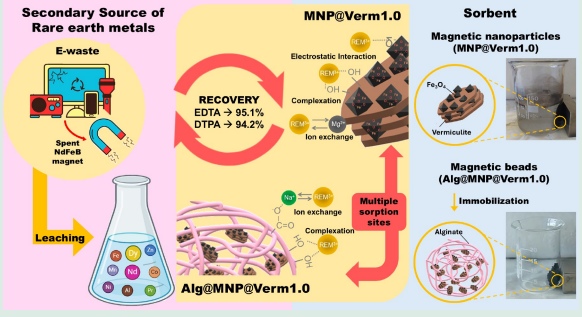

ABSTRACT: Rare Earth Metals (REMs) are vital for advanced technologies, yet they face increasing supply risks, emphasising the need for efficient recovery from secondary resources such as NdFeB magnet waste. The present work details the development and characterisation of magnetically responsive vermiculite-based nanocomposites, with and without alginate immobilisation, aimed at the selective recovery of neodymium (Nd(III)) and dysprosium (Dy(III)) ions from synthetic solutions and real NdFeB magnet leachate. The composites were synthesised by incorporating Fe_3O_4 nanoparticles into vermiculite, and, in some cases, the resulting material was encapsulated in alginate beads. X-ray diffraction was utilised to confirm the formation of magnetite, while the magnetic responsiveness of all sorbents was sufficient for straightforward separation. The presence of additional functional groups, including hydroxyl, carboxyl, and silicate, was shown to enhance sorption performance. Although alginate immobilization significantly reduced sorption kinetics, it led to higher sorption capacities and enhanced structural stability. Non-immobilised materials exhibited greater selectivity for Nd(III) over Dy(III), a critical challenge in the separation of REMs. Regeneration studies confirmed the efficient metals desorption when complexing agents were utilised. The high sorption performance of these low-cost and eco-friendly nanocomposites in real leachate systems demonstrates their applicability for sustainable REM recovery from e-waste streams.

✉ Corresponding authors. E-mails: claudia.b.lopes@ua.pt (C. Lopes); melissag@unicamp.br (M. Vieira)
Article history: Received 31 July 2025, Revised 16 December 2025, Accepted 18 December 2025, Available online 30 January 2026

KEYWORDS: Magnetic nanoparticles, Alginate, Rare earth metal, Recovery, Sorption

1 Introduction

Rare earth metals (REMs) are scarce and strategically important resources for the green energy sector (Filho et al., 2023). Elements such as neodymium and dysprosium are essential for manufacturing NdFeB magnets, which are used in equipment and technologies like hard drives and wind turbines. Furthermore, these elements are considered among the most critical rare earth metals due to their supply risk and significance for clean energy (Cardoso et al., 2019). The scarcity and strategic importance of these elements have driven research into REMs recovery technologies within the context of the circular economy (Depraiter and Goutte, 2023).

In this context, secondary sources, such as electronic waste and industrial by-products, are crucial to the circular economy of REMs, as they provide a sustainable alternative to primary mining, while reducing environmental impacts and supply chain risks (Jyothi et al., 2020). Among secondary sources, leachates from hard drives and electronic waste are particularly promising due to their high metal concentration, that offers environmental and economic advantages, often exceeding those found in ores (Vuppaladadiyam et al., 2024). Sorption processes, integrated into hydrometallurgical routes for recovering REMs from NdFeB magnet scraps, are effective at low concentrations and are direct, efficient, and cost-effective (de Vargas Brião et al. 2022).

Several studies have investigated the sorption of individual REMs. However, only a few sorbents have been applied to concentrate and recover REMs from magnet-waste leachates, such as sodium polyacrylate core-shell fibers and nanoporous zeolitic imidazolate-8 framework nanocrystals (Jung et al. 2024), green microalgae (Kucuker et al., 2017), bifunctional mesoporous silica (Dudarko et al., 2022), EDTA-functionalized chitosan (Srivastava et al., 2024), alginate beads (Emil-Kaya et al., 2024), and vermiculite (de Vargas Brião et al. 2024). Despite the efficient removal of REMs by these sorbents, the main challenge faced by sorption-based separations is selectivity. To overcome this, promising strategies such as surface functionalization (Dudarko et al., 2022; Srivastava et al., 2024) and selective desorption processes (de Vargas Brião et al., 2024; Jung et al., 2024) have been proposed. Another common challenge is the overall stability of sorbents, which must resist degradation over multiple use cycles, thereby improving the economic viability and sustainability of the process (de Vargas Brião et al., 2022). According to Xiang et al. (2025), biopolymers, carbon-based materials, and nanomaterials have shown promising potential for reuse due to their easy combination with other materials and biodegradability, thereby enhancing the stability of the final sorbent without compromising the safety or environmental compatibility of its disposal.

Among these, vermiculite, a clay mineral, offers several advantages including low cost, wide availability, high cation exchange capacity, and chemical stability (Feng et al., 2020). Magnetic nanoparticles (MNPs) are promising sorbents for the recovery of REMs from wastewater due to their high adsorption capacity, large specific surface area, selective sorption enabled by surface functionalization, and efficient reuse via magnetic separation (Kegl et al., 2020; Molina-Calderón et al., 2022). Recently, various types of magnetic nanoparticles have been proposed for removing REMs from aqueous solutions, such as calmodulin-functionalized magnetite silica nanoparticles (NPs) (Ye et al., 2023), hematite NPs (Zhao et al., 2024), and functionalized mesoporous magnetite silica (Li et al., 2018).

Despite these advantages, MNPs face challenges such as self-aggregation behaviour of nanosized particles (Lu, 2012) and low reusability due to iron leaching during sorption and desorption cycles (Artiushenko et al., 2023). For this reason, MNPs are often coated with a polymer layer or immobilized within a polymeric matrix. Biopolymers have been investigated as matrices for immobilizing MNPs that meet sustainability and renewability criteria, while enhancing sorption capacity through the wide variety of functional groups in the final composite, such as hydroxyl, amine, and carboxyl groups (de Vargas Brião et al., 2020).

Several low-cost, widely available biopolymers have been employed to produce biocomposites incorporating iron-based MNPs, including cellulose (Rahmatika et al., 2020), lignin (Gautam et al., 2024), starch (Rakotomalala Robinson et al., 2023), carrageenan (Macedo et al., 2022), chitosan (González-Martínez et al., 2021), and alginate (Kloster et al., 2020). Among these, alginate, an anionic linear polysaccharide, is well known for its simple procedure to form homogeneous spherical beads through ionic crosslinking (Ciarleglio et al., 2023) and has demonstrated excellent performance in the removal of REMs from aqueous solutions (da Costa et al., 2021).

Thus, this study aims to investigate the effect of vermiculite content on magnetic nanoparticles, either immobilised or not within alginate spheres, on the efficiency of REMs removal and recovery from NdFeB magnet leachate. Through this approach, this study seeks to develop advanced and innovative sorbents that provide a sustainable and cost-effective alternative for REMs recovery, thereby addressing the critical scarcity of these resources and supporting the circular economy of these strategically important materials.

2 Materials and methods

2.1 Chemicals and materials

The chemicals and materials used in this work are listed in the Supporting Information.

2.2 Sorbent synthesis

2.2.1 MNP@VermX

Expanded vermiculite was first crushed in a ball mill and sieved. The fraction retained on a 400-mesh sieve (0.037 mm opening) was collected. Next, the magnetic nanocomposite (MNP@VermX) was synthesised by adapting the method proposed by Schwertmann and Cornell (2000) for the synthesis of magnetite nanoparticles via oxidative hydrolysis, with vermiculite powder added in different proportions to the reaction medium. The procedure (Fig. 1(a)) involved dissolving 1.90 g of potassium hydroxide and 1.52 g of potassium nitrate in 25 mL of deoxygenated water (previously purged with N_2 for 2 h) at 60 °C under continuous nitrogen flow with stirring at 500 r/min. Then, a mixture of 4.73 g of iron sulfate heptahydrate and 0.2, 0.6 or 1.0 g of vermiculite was added dropwise to the alkaline medium, and the stirring speed was increased to 700 r/min for 30 min. Afterward, the solution was heated to 90 °C for 4 h under a nitrogen atmosphere without stirring. The final product was then magnetically separated, washed with deoxygenated water and ethanol and subsequently dried at 40 °C. The resulting samples were labelled as "MNP@VermX", where X represents the mass of vermiculite used in the synthesis (0.2, 0.6 or 1.0 g).

2.2.2 Alg@MNP@Verm1.0

MNP@Verm1.0 exhibited the most effective sorption of Nd(III) and Dy(III) (method described in Section 2.4.2.1) and was selected for the preparation of

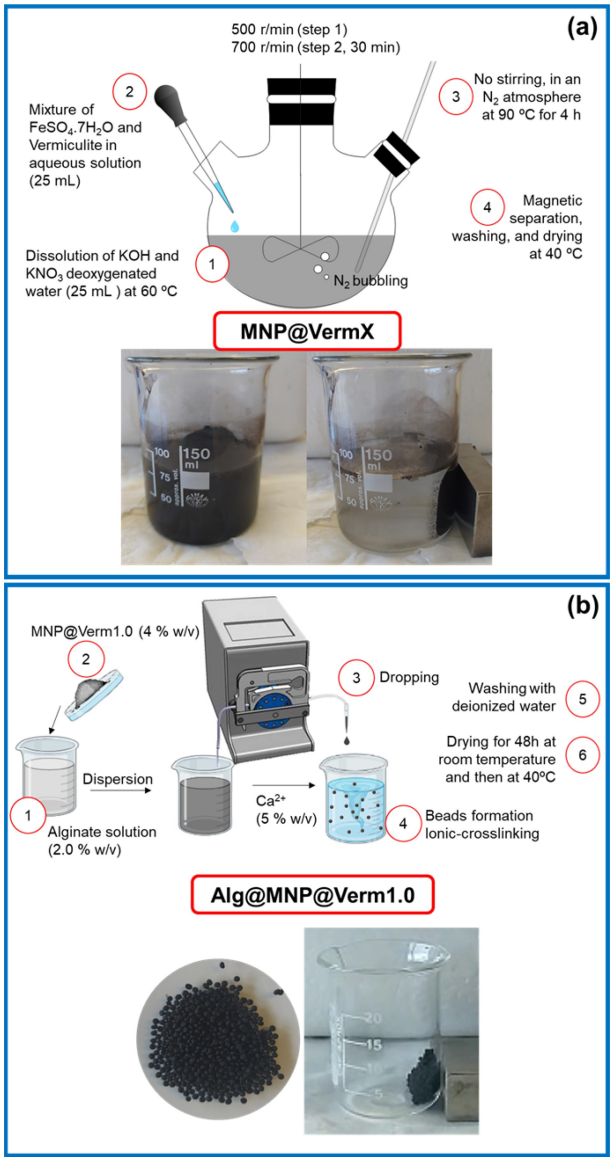

Fig. 1 Schematic representation of the synthesis route of MNP@VermX (a) and Alg@MNP@Verm1.0 nanocomposites (b).

vermiculite-alginate magnetic beads via ionic crosslinking (da Costa et al., 2022). Specifically, an aqueous alginate solution (2%, w/v) was prepared by dissolving 0.5 g of the biopolymer in 25 mL of deionized water under continuous magnetic stirring at 1000 r/min for 30 min. Subsequently, 1.0 g of MNP@Verm1.0 nanoparticles was dispersed in the alginate solution using a glass impeller. The dispersion was then homogenized in an ultrasonic bath to eliminate air bubbles. Next, the solution was continuously dripped into a 5 % (w/v) $CaCl_2$ solution under magnetic stirring until a vortex formed. A peristaltic pump was used for dripping, with the hose

attached to the tip of a pipette to produce uniform drops (Fig. 1(b)). The resulting hydrogels were dried at room temperature for 72 h. The magnetic beads were labelled as Alg@MNP@Verm1.0.

2.3 Sorbents characterization

The magnetic saturation curves (VSM) of all MNP@VermX and Alg@MNP@Verm1.0 samples were obtained using a superconducting quantum interference device (SQUID) magnetometer (Quantum Design, USA). Isothermal magnetization (M) as a function of the applied magnetic field (H) was measured at 5 K, 300 K, and 380 K. Geometric effects were corrected according to the method described by Amorim et al. (2021).

The crystallinity of the MNP@VermX and Alg@MNP@Verm1.0 samples was evaluated by X-ray diffraction (XRD) using a PANalytical Empyrean X-ray diffractometer (PANalytical, Almelo, Netherlands) with the CuKα monochromatic radiation operated at 45 kV and 40 mA.

The functional groups of MNP@VermX and Alg@MNP@Verm1.0 were identified by diffuse reflectance infrared Fourier transform spectrometry (DRIFT) using a Jasco FT/IR 4X spectrometer (Japan). The samples were scanned at a resolution of 4 cm^{-1} over the wavelength range of 349–4000 cm^{-1}, and the spectra were expressed in Kubelka-Munk units.

The morphologys of both samples were examined using scanning electron microscopy coupled with energy dispersive spectroscopy (SEM-EDS) (LEO Electron Microscopy, UK).

Thermal stability was evaluated by thermogravimetric and differential thermal analyses (TGA/DTA) using a DTG-60 system (Shimadzu, Japan). The analyses were performed under nitrogen atmosphere (50 mL/min) with a heating rate of 20 °C/min.

The zeta potential of the samples was determined using a Malvern Zetasizer Nano ZS (Malvern Instruments, UK) by electrophoretic light scattering. The samples, MNP@Verm1.0 and milled Alg@MNP@Verm1.0, were dispersed in ultrapure water, and the pH of the suspensions was adjusted by the addition of 0.1 mol/L HNO_3 or 0.1 mol/L NaOH. Measurements were performed at 25 °C using disposable capillary cells (DTS1070). For each pH value, at least three independent measurements were performed, and the results are reported as mean ± standard deviation. Electrophoretic mobility was converted to zeta potential using the Smoluchowski approximation.

The Nd(III)- and Dy(III)-loaded materials (loaded-MNP@Verm1.0 and loaded-Alg@MNP@Verm1.0) were analysed by X-ray photoelectron spectroscopy (XPS) (Thermo Scientific, Czech Republic), in which the Al Kα line energy was 1486.6 eV, operated at a base pressure of 7×10^{-8} mbar with a 200 µm spot size. Survey spectra were acquired over 10 scans at a resolution of 0.50 eV, and elemental analysis by 15 scans with a resolution between 0.1 and 0.5 eV.

2.4 Sorption

2.4.1 General aspects

Sorption experiments were conducted in batch. A sorbent dosage of 0.1 g/L was used with binary or multi-metal solutions under stirring at 200 r/min for 24 h. The tests were performed at room temperature in an orbital shaker (ZWYR-240, Labwit, Australia), except the kinetic studies were carried out under mechanical agitation to collect aliquots over time. The pH was adjusted to 3.5 ± 0.1 by adding small volumes of 0.1 mol/L nitric acid.

After each experiment, the sorbent was separated using an external magnetic field, and the liquid aliquots were filtered with syringe filters (Chromafil Xtra, 0.20 µm porous). Subsequently, 25 µL of 65 % HNO_3 was added to each aliquot to preserve the samples prior to analysis. The initial and final metals concentrations were measured using Inductively Coupled Plasma Mass Spectrometry (ICP-MS, Agilent 7700, USA). The sorption efficiency parameters evaluated in this study are the removal percentage (R) and sorption capacity (q), calculated by Eqs. (1) and (2):

$$R = \frac{C_0 - C}{C_0} \times 100\%, \quad (1)$$

$$q = \frac{C_0 - C}{C_s}, \quad (2)$$

where C_0 is the initial concentration (µmol/L) of the metal ions, C is the concentration at any time t, and C_s is the sorbent dosage (g/L).

2.4.2 Binary study

Sorption studies were carried out using equimolar solutions of Nd(III) and Dy(III) at a concentration of 10 µmol/L. The working solutions were prepared from stock solutions obtained by dissolving 5 g of neodymium(III) or dysprosium(III) nitrate hydrate in 100 mL of ultrapure water.

This study investigated the effect of vermiculite content on the sorptive response of magnetic nanocomposites in the Nd(III)/Dy(III) system using

MNP@VermX sorbents. After identifying the optimal magnetic sorbent, the performances of both alginate-immobilized and non-immobilized sorbents were assessed in terms of the pH effect, sorption kinetics, equilibrium and desorption ability.

The effect of pH on the sorption efficiency of MNP@Verm1.0 and Alg@MNP@Verm1.0 was evaluated by varying the initial pH from 1.0 to 6.0, by adding nitric acid to the solutions. This pH range was defined based on the simulated metal speciation in aqueous solution using Visual Minteq 3.1.

Sorption kinetics were assessed by collecting aliquots at predetermined time intervals. Experimental data were fitted to reaction- and diffusion-based kinetic models using nonlinear regression, specifically the pseudo-first order (PFO, Eq. (S1)) (Lagergren, 1898), pseudo-second order (PSO, Eq. (S2)) (Ho and McKay, 1998, 1999), Elovich (Eq. (S3)) (Aharoni and Tompkins, 1970; Wu et al., 2009), Weber and Morris (Weber and Morris, 1963) (Eq. (S4)), and Boyd models (Eqs. (S5)–(S9)) (Boyd et al., 1947; Viegas et al., 2014) .

Sorption equilibrium studies were conducted using equimolar binary solutions with fixed initial concentration (10 μmol/L for each element) and varying sorbent dosage, at 25 °C. Samples were collected at the beginning and after 24 h of contact, acidified and analysed by ICP-MS. Equilibrium data were modelled using two- and three-parameter models: Freundlich (Eq. (S10)) (Freundlich, 1906), Langmuir (Eq. (S11)) (Langmuir, 1918), Dubinin-Radushkevich (Eqs. (S12)–(S14)) (Dubinin and Radushkevich, 1947), Brunauer-Emmett-Teller (BET, Eq. (S15)) (Brunauer et al., 1938), Sips (Eq. (S16)) (Sips, 1948) and Toth (Eq. (S17)) (Tóth, 1995, 1997). Details of the equations and the fitting methodology are provided in the Supplementary Material.

Desorption studies were conducted to evaluate the performance of six eluents: NH_4Cl, $MgCl_2{\cdot}6H_2O$, DTPA, $Na_2EDTA{\cdot}2H_2O$, HNO_3, and HCl. The loaded sorbents were prepared by contacting 0.1 g/L of MNP@Verm1.0 and Alg@MNP@Verm1.0 with binary solutions (pH 3.5 ± 0.1) under stirring at 200 r/min for 24 h. Then, aliquots of 10.0 mg of the loaded sorbents were contacted with 0.1 L of each solution (0.01 mol/L) for 24 h. The Nd(III) and Dy(III) concentrations in the eluates were analysed by ICP-MS. Desorption efficiency was evaluated based on the difference in sorbed phase concentration (Δq, μmol/g) (Eq. (3)) and desorption efficiency (D, %) (Eq. (4)).

$$\Delta q = \frac{C_E}{C_s}, \tag{3}$$

$$D = 100\frac{\Delta q}{q}, \tag{4}$$

where C_E is the metal concentration in the eluate solution (μmol/L).

2.4.3 Leachate of permanent magnets NdFeB

The efficiency of the sorbents (MNP@Verm1.0 and Alg@MNP@Verm1.0) for concentrating REMs from an NdFeB magnet leachate was evaluated by mixing 0.1 g/L of each sorbent with a simulated leachate solution (pH 3.6) containing 7.27 mmol/L Fe(III), 0.034 mmol/L Al(III), 0.026 mmol/L Ni(II), 0.43 mmol/L Zn(II), 0.12 mmol/L Co(II), 0.015 mmol/L Mn(II), 0.048 mmol/L Dy(III), 0.74 mmol/L Nd(III), and 0.26 mmol/L of Pr(III) at 22 °C. The leachate composition was prepared following Brewer et al. (2019), where NdFeB magnetic scrap was leached with sulfuric acid (1 mol/L).

After 24 h, the sorbents were washed with ultrapure water, dried at 40 °C, and subsequently immersed in the most effective eluents identified in the binary sorption study. The metals concentrations in the eluates were measured using inductively coupled plasma optical emission spectrometry (ICP-OES) using a Perkin-Elmer Optima 4300 DV spectrometer (USA).

The sorptive performances of the sorbents were determined from the concentration of each metal in the sorbed phase, according to Eq. (1).

2.5 Assessment of data correlation quality

The adjusted coefficient of determination (R^2_{adj}) (Eq. (S18)), the standard deviation of the residuals ($S_{y,x}$) (Eq. (S19)), and the Akaike information criterion (AIC) (Eq. (S20)) were used to assess the quality of fit of the kinetic and equilibrium models (Simonin, 2016; Tan and Hameed, 2017; Wang and Guo, 2020). Nonlinear regression was performed using GraphPad Prism 10.4.0 software. Details are provided in the Supplementary Material.

3 Results and discussion

3.1 Characterization of sorbents

Figure 2 shows the magnetic saturation curves (VSM) of the MNP@VermX nanocomposites and the Alg@MNP@Verm1.0 spheres. The curves provide key parameters, including the saturation magnetization (M_{sat}) and coercive field (Hc) (Table 1).

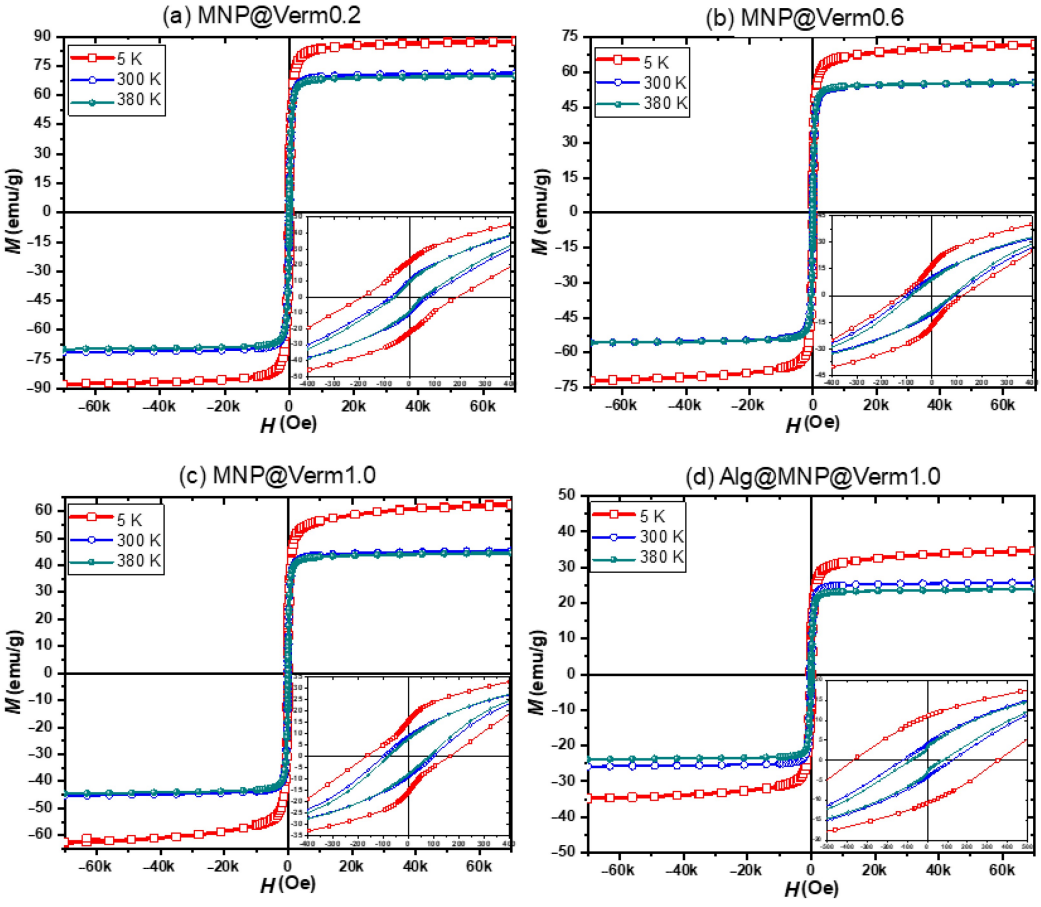

Fig. 2 Magnetization as a function of the applied magnetic field at 5 K, 300 K, and 380 K for MNP@Verm0.2 (a), MNP@Verm0.6 (b), MNP@Verm1.0 (c), and Alg@MNP@Verm1.0 (d). The inset shows new measurements made with the remaining coil field removed/corrected, except for the 5 K cure, for which the high coercivity required a direct magnified view of the original data.

The hysteresis observed in the VSM curves confirms that the samples exhibit ferromagnetic or ferrimagnetic behaviour (Ghasemi, 2022). This indicates that the MNP have sizes exceeding the critical threshold for a single magnetic domain, leading to ferromagnetic or ferrimagnetic properties rather than superparamagnetism (Callister and Rethwisch, 2018). Furthermore, MNPs intercalated within the MNP@Vermiculite nanocomposites tend to exhibit combined ferro-ferrimagnetic behaviour due to the elongated morphology of the nanoparticles within the clay layers (Chen et al., 2016).

Table 1 shows that the M_{sat} values of the samples decreased with increasing vermiculite and alginate content in the nanocomposites. At room temperature, the M_{sat} value decreased from 71 emu/g for MNP@Verm0.2 to 45 emu/g for MNP@Verm1.0, and further dropped to 25.8 emu/g for Alg@MNP@Verm1.0 due to the higher content of non-magnetic compounds, resulting from the addition of alginate. Despite this reduction, all samples exhibited sufficient magnetization to enable easy separation from the solution using an external magnetic field, confirming the practical applicability of both MNP@VermX and Alg@MNP@Verm1.0.

Unlike M_{sat}, which depends primarily on material composition, the coercivity depends on structural variables rather than chemical composition (Callister and Rethwisch, 2018). Structural defects, such as non-magnetic phases or voids, can hinder domain-wall motion, thereby increasing Hc. Consequently, the incorporation of non-magnetic components such as vermiculite or alginate typically enhances coercivity. As expected, M_{sat} values increased at lower temperatures. This behaviour is attributed to the decrease in thermal agitation as the temperature approaches 0 K, allowing dipole moments to align more completely and reach maximum magnetization

Table 1 Magnetic parameters of MNP@VermX and Alg@MNP@Verm1.0 nanocomposites

Sample	T (K)	M_{sat} (emu/g)	–Hc (Oe)	+Hc (Oe)
MNP@Verm0.2	5	87 ± 2	–185 ± 2	185 ± 2
	300	71 ± 1	–70 ± 2	71 ± 2
	380	70 ± 1	–58 ± 2	55 ± 2
MNP@Verm0.6	5	72 ± 1	–139 ± 2	138 ± 2
	300	56 ± 1	–102 ± 2	87 ± 2
	380	56 ± 1	–84± 2	83 ± 2
MNP@Verm1.0	5	63 ± 1	–190 ± 2	176 ± 2
	300	45 ± 1	–102 ± 2	99 ± 2
	380	45 ± 1	–82 ± 2	81 ± 2
Alg@MNP@Verm1.0	5	34.8 ± 0.4	–372 ± 15	352 ± 15
	300	25.8 ± 0.3	–125 ± 2	123 ± 3
	380	24.0 ± 0.3	–83 ± 2	75 ± 3

regardless of the applied field strength.

Figure 3(a) shows the characteristic diffraction peaks of vermiculite and Fe_3O_4 in all MNP@VermX nanocomposites. Even in the Alg@MNP@Verm1.0 spheres, some diffraction peaks associated with Fe_3O_4 were still identified. The peaks corresponding to the 1.43 nm (002) basal spacing, typical of vermiculite in accordance with the ICDDPDF file no. 01-076-6603 (Valášková et al., 2022), and those related to the (008) plane became more pronounced with increasing vermiculite content in the samples. However, the characteristic (002) reflection is observed as a shoulder of the peak at around 8.2 degrees (1.07 nm), which is atypical for the vermiculite structure. This behaviour may result from the exchange of K^+ with Mg^{2+} ions in the interlayer during MNP synthesis, leading to a contraction of the vermiculite basal spacing to 1.07 nm (Malla, 1978; Delarmelinda et al., 2017). At low vermiculite contents, the vermiculite interlayer becomes fully saturated with K^+, resulting in the disappearance of the (002) reflection (Dubus et al., 2023).

The characteristic diffraction peaks of Fe_3O_4 were observed at higher diffraction angles than those of vermiculite. The diffraction peaks at 2θ values of 18.3°, 30.2°, 36.5°, 38.2°, 42.9°, 53.8°, 57.3°, and 63.2° correspond to the crystal planes of (111), (220), (311), (222), (400), (422), (511) and (440), respectively, of the iron oxide cubic phase (ICDDPDF file No. 04-013-7099), confirming the presence of magnetite (Ancira-Cortez et al., 2017; Rahman et al., 2017; Bugarčić et al., 2021).

The Alg@MNP@Verm1.0 spheres exhibit a diffractogram with less intense peaks compared with the respective non-immobilized sorbent (MNP@) Verm1.0), which reflects the amorphous nature of the polysaccharide alginate (Marangoni Júnior et al., 2021) with some crystalline structures associated with the MNP@Verm1.0 content.

Figure 3(b) shows the FT-IR drift spectra of the MNP@VermX nanocomposites. The spectra show a strong peak characteristic of Si−O stretching vibrations in the tetrahedral silicate layers of the vermiculite structure, and the peak attributed to Fe−O stretching (594 cm^{-1}) of magnetite, whose intensity increases as the amount of vermiculite in the composite decreases.

Figure 3(c) shows the FT-IR drift spectra of the non-alginate sorbent (MNP@Verm1.0) and the alginate-immobilized sorbent (Alg@MNP@Verm1.0). The main differences between the two spectra are the peaks and bands corresponding to different functional groups of the alginate present in Alg@MNP@Verm1.0, including: a broad band centered at 3282 cm^{-1} due to O−H stretching vibrations of the hydroxyl groups in the alginate structure; a strong peak at 1604 cm^{-1}, attributed to the asymmetric stretching vibrations of the carboxylate groups; and another peak at 1422 cm^{-1}, associated with the symmetric stretching of the same functional group (COO−); some peaks in the region between 1000–1270 cm^{-1} corresponding to the C−O and C−C stretching vibrations in the alginate polysaccharide structure; and a small peak at 1310 cm^{-1} assigned to the bending vibrations of the O−H groups.

Other features present in both spectra include a prominent peak characteristic of Si−O stretching vibrations in the tetrahedral silicate layers of the vermiculite structure, observed at 1003 cm^{-1} in MNP@Verm1.0 and slightly shifted to 1006 cm^{-1} in Alg@MNP@Verm1.0. The peaks at 813 cm^{-1} in MNP@Verm1.0 and 819 cm^{-1} in Alg@MNP@) Verm1.0 can be attributed to bending vibrations of

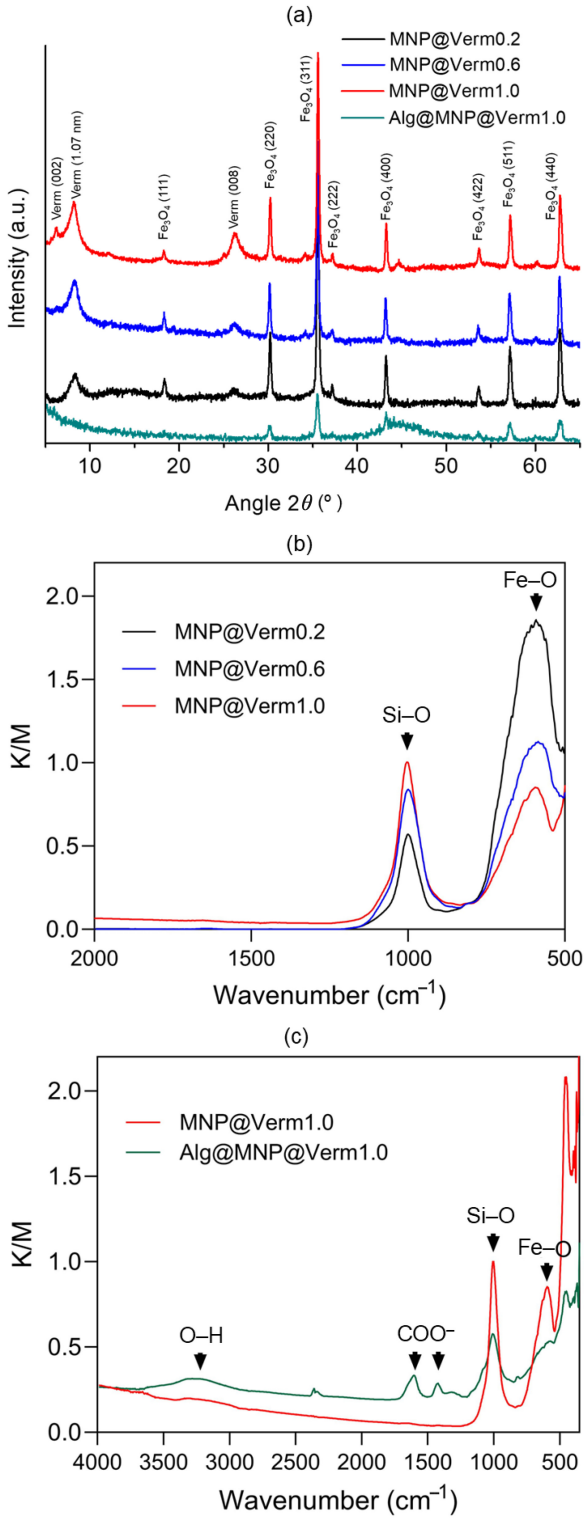

Fig. 3 X-ray diffractograms (a) and FT-IR drift spectra of the non-immobilized magnetic nanocomposites with different vermiculite contents (MNP@VermX) (b) and of the non-immobilized magnetic alginate composites containing 1.0 g of vermiculite (MNP@Verm1.0 and Alg@MNP@Verm1.0) (c).

Al–O within the octahedral vermiculite layers. In addition, peaks at 629 and 450 cm^{-1} are associated with the bending vibrations of Si–O–Si and Si–O–Al bonds in the silicate framework of vermiculite. In the MNP@Verm1.0 spectrum, the identified peaks at 594, 383, 372, and 351 cm^{-1} are attributed to the Fe–O stretching and Fe–O bending vibrations of magnetite nanoparticles. These peaks are shifted to 573 and 392, 379, and 368 cm^{-1} in the alginate-immobilized sorbent.

The FT-IR spectra of the two sorbents reveal prominent characteristic peaks of specific functional groups of magnetite, vermiculite and alginate, confirming the preservation of their structural features in the non-immobilized and alginate-immobilized sorbents, respectively. Minor shifts in the positions and intensities of these peaks are attributed to the synthesis process of the nanocomposites.

The morphologies of both nanocomposites were examined by scanning electron microscopy, as shown in in Fig. 4.

The MNP@Verm1.0 nanocomposite exhibits a heterogeneous character with particles of variable sizes and shapes and a rough surface (Fig. 4(a)). At higher magnification (Fig. 4(b)), the layered structure of expanded vermiculite with aggregates of magnetite nanoparticles is observed, along with a high degree of roughness and porosity.

The Alg@MNP@Verm1.0 nanocomposite consists of spheres with diameters of about 1 mm (Fig. 4(c)). Although the surface is rough (Figs. 4(d) and 4(e)), the alginate-immobilized sorbent exhibits a higher degree of homogeneity than the non-immobilized one, due to the presence of the polymer. Upon fracture of the spheres, vermiculite layers in different orientations are visible, together with aggregates of magnetite nanoparticles (Fig. 4(f)). Elemental analysis of both composites indicates the presence of all elements expected for expanded vermiculite (Mg, K, Fe, Si, Al, O) and magnetite (Fe, O) (Table S3, Supplementary Material).

Furthermore, in Alg@MNP@Verm1.0, the presence of carbon and increased oxygen content is due to alginate. In addition, Ca and Cl in Alg@MNP@Verm1.0 result from the use of calcium chloride as crosslinker in the synthesis of the composite. With the exception of oxygen, whose proportion increases, the relative content of the other elements in Alg@MNP@Verm1.0 decreases compared with MNP@Verm1.0 due to the presence of alginate. However, the proportions of the primary metals in vermiculite remain nearly constant in both composites, confirming the unchanged structure of the clay.

Figures 5(a) and 5(b) show the thermogravimetric

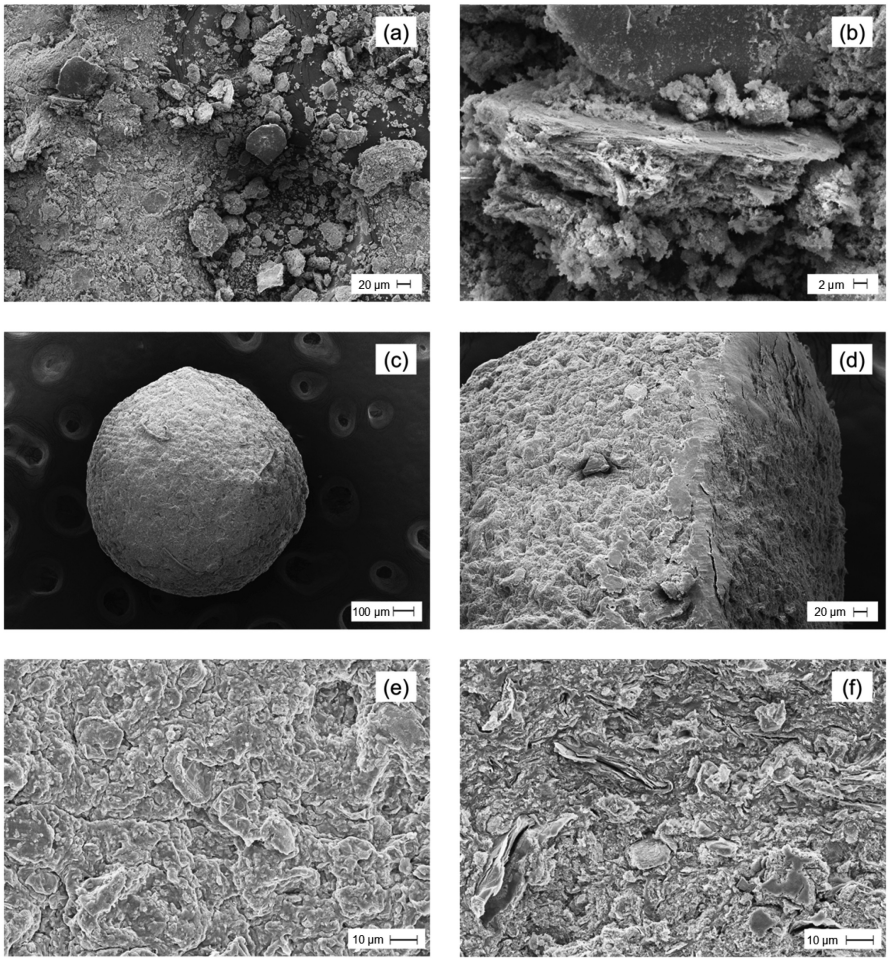

Fig. 4 SEM images of MNP@Verm1.0 at magnifications of 500× (a) and 5k× (b), and Alg@MNP@Verm1.0 at magnifications of 150× (c), 500× (d) and 2k× of the external surface (e), and of the fracture (f).

(TGA) and differential thermal (DTA) analyses of MNP@Verm1.0andAlg@MNP@Verm1.0,respectively, carried out in an air atmosphere.

The mass loss of MNP@Verm1.0 in the temperature range of 30 to 1000 °C is primarily attributed to the loss of water. However, a slight mass increase observed between 140 and 220 °C is related to the oxidation of Fe_3O_4 to γFe_2O_3 (Liang and Lu, 2020), which is accompanied by an endothermic peak in the DTA curve. Another DTA peak, observed between 720 and 800 °C, corresponds to the transition to αFe_2O_3 (Monazam et al., 2014). The effect of temperature on the vermiculite content in this temperature range is also related to the loss of chemical structural water through a dehydroxylation reaction. Thermal decomposition above 800 °C leads to the formation of compounds such as forsterite, mullite, and alumina (Feng et al., 2020). The total mass loss of the MNP@vermiculite nanocomposites was only 5 %.

Figure 5(b) shows that the initial mass loss (around 8%) up to 200 °C corresponds to dehydration and loss of volatiles. In the range of 200–580 °C, the alginate content undergoes thermal degradation in two distinct steps (Pawar et al., 2020). This process involves the cleavage of carbon chains and the formation of carbonates (da Silva Fernandes et al., 2018). The complete oxidation of the carbonates results in a slight endothermic peak, with a minimum at 790 °C. Above 800 °C, the final degradation products remain stable up to 1000 °C (Kragović et al., 2016). The final mass loss of Alg@MNP@Verm1.0 was 40%, primarily attributed to alginate degradation.

3.2 Sorption of neodymium and dysprosium from binary solutions

3.2.1 Vermiculite effect

Figure 6 shows the effect of vermiculite content on the

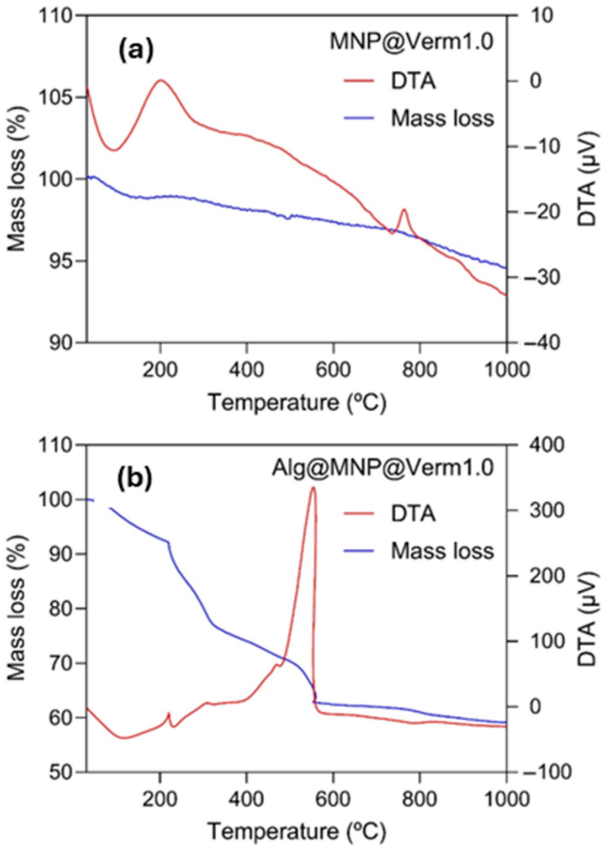

Fig. 5 TGA and DTA of MNP@Verm1.0 (a) and Alg@MNP@Verm1.0 (b) nanocomposites.

sorption performance of the magnetic nanocomposites. The results clearly demonstrate that the increase in vermiculite content enhances the sorption capacity of the magnetic nanocomposite.

MNP@Verm1.0 achieved the highest sorption uptake, 63.0 μmol/g for Nd(III) and 43.9 μmol/g for Dy(III). Vermiculite has a known cation exchange capacity of around 1.43 mmol/g (de Vargas Brião et al., 2021), which enhances the sorption capacity of single magnetite nanoparticles. Based on these excellent results, MNP@Verm1.0 was selected to synthesise magnetic alginate beads, Alg@MNP@Verm1.0, a novel magnetic bionanocomposite.

3.2.2 pH effect

The pH of the medium is one of the most critical factors in the sorption of charged adsorbates (Hisada and Kawase, 2018; da Costa Costa et al., 2020), as it can influence the speciation of ions in solution that are attracted or repelled from the adsorbent surface. Figure 7 shows the effect of pH on the sorption uptake of magnetic nanocomposites with and without alginate immobilization.

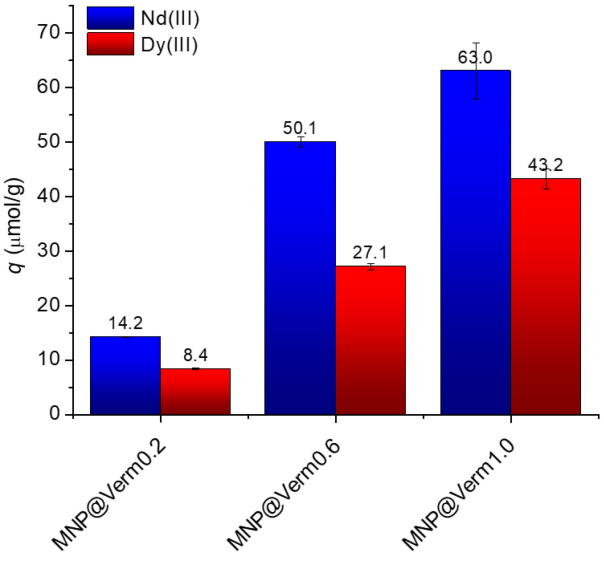

Fig. 6 Effect of vermiculite content on the sorption capacity of magnetic nanoparticles towards Nd(III) and Dy(III). Experimental conditions: $C_{Nd(III)} = C_{Dy(III)} = 10$ μmol/L; $C_S = 0.1$ g/L; stirring at 200 r/min; contact time of 24 h; pH 3.5 ± 0.1.

For both sorbents, the sorption uptake increased with increasing pH because, at higher pH, there is less competition with H^+ ions. MNP@Verm1.0 showed different sorption uptake values for each metal, especially in the pH range of 2.0–5.0 where Nd(III) was preferentially sorbed over Dy(III). This behaviour was not observed for the Alg@MNP@Verm1.0 spheres, where the sorption uptake values for both metals were practically the same, except at pH 2.0.

Despite the best performance at high pH, a pH of approximately 3.6 was selected for the kinetics and equilibrium studies, as it corresponds to the pH of the magnetic scrap leachates used as references in this study (Brewer et al., 2019). At this pH, the sum of the sorbed amounts of the two metals on each sorbent is 116.2 and 136.5 μmol/g for MNP@Verm1.0 and Alg@MNP@Verm1.0, respectively. This superior overall performance of Alg@MNP@Verm1.0 compared to MNP@Verm1.0 is intrinsically related to its more negatively charged surface (Fig. 7(c)). At the operating pH (3.6), the zeta potentials of the nanocomposites were around −4 and −19 mV, for MNP@Verm1.0 and Alg@MNP@Verm1.0, respectively.

3.2.3 Kinetics

The sorption kinetic profiles of Nd(III) and Dy(III) on MNP@Verm1.0 and Alg@MNP@Verm1.0 nanocomposites are shown in Fig. S1 (Supplementary Material)

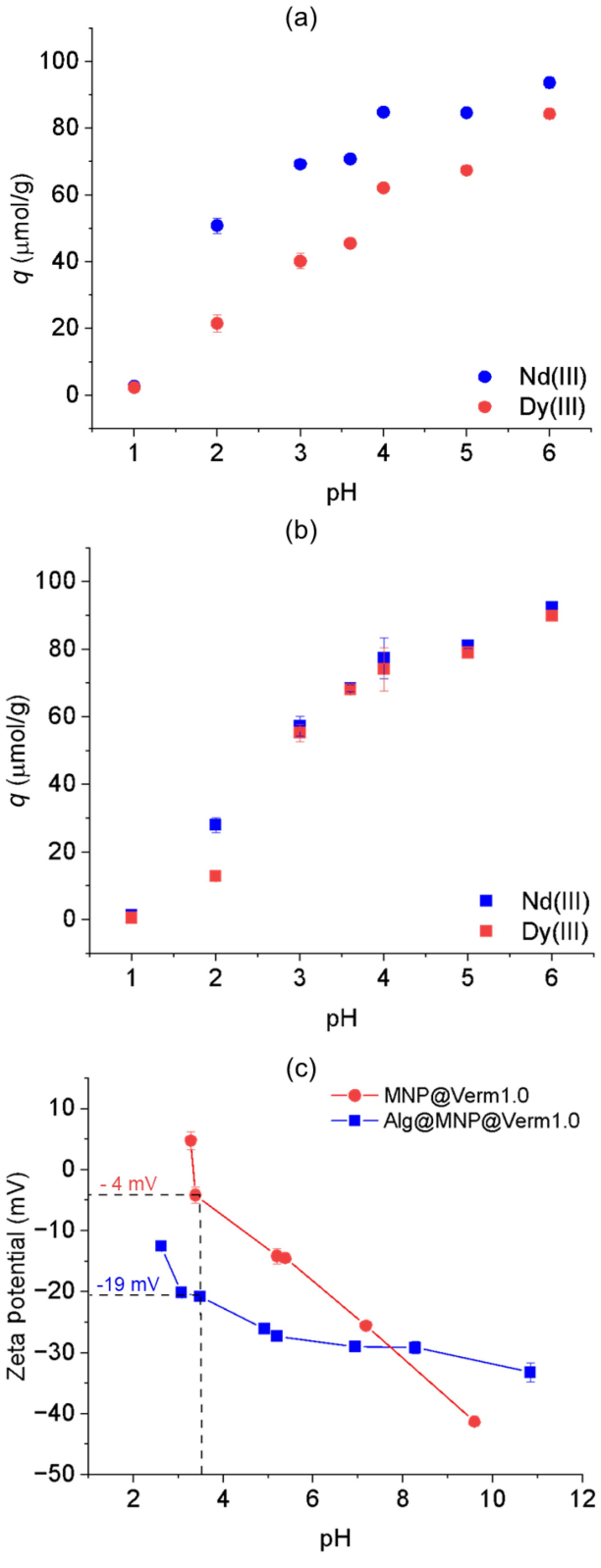

Fig. 7 Effect of pH on the Nd(III) and Dy(III) uptake of MNP@Verm1.0 (a) and Alg@MNP@Verm1.0 (b) nanocomposites; Zeta potential of samples as a function of pH (c).

alongside the fits to the reaction models (PFO, PSO, and Elovich) and diffusion models (Weber and Morris, and Boyd), while the best-fit parameters and the quality of the fits are provided in Table S4. The REMs sorption kinetics of the REMs on the two nanocomposites are significantly different.

For the Nd(III)/Dy(III):MNP@Verm1.0 system, a steep increase in the amount of metals sorbed per mass of sorbent (q_t, μmol/g) is observed within the first hour, followed by a slower sorption rate until equilibrium is reached (Fig. S1(a)). In contrast, the Nd(III)/Dy(III): Alg@MNP@Verm1.0 system shows an almost linear and continuous increase in q_t values throughout the duration of the sorption assay (Fig. S1(b)). Moreover, the kinetics of REMs sorption on MNP@Verm1.0 are much faster than those on Alg@MNP@Verm1.0, with equilibrium being reached at about 180 min for MNP@Verm1.0, whereas 1440 min were still insufficient to reach equilibrium for Alg@MNP@ Verm1.0. Another interesting result concerns the non-coincident pattern of q_t values for Nd(III) and Dy(III) on the MNP@Verm1.0 nanocomposite, which led to different equilibrium values for Nd(III) and Dy(III): 67.1 and 44.6 μmol/g, respectively, in contrast to the coincident pattern observed for the Alg@MNP@ Verm1.0, which resulted in similar q_e values (68.4 and 68.0 μmol/g, for Nd(III) and Dy(III)). These results suggest that MNP@Verm1.0 shows selectivity towards Nd(III), whereas Alg@MNP@Verm1.0 does not differentiate between the two metals. This was confirmed by the equilibrium selectivity values for both sorbents, 2.49 and 1.06, respectively. These values were calculated as the ratio of the partition coefficients of each element, where the partition coefficient is defined as the ratio of the solid phase concentration, q_e, to the solution concentration, C_e (Cardoso et al., 2013).

In this study, it was observed that the PSO model fits the data better than the PFO model for Nd(III) and Dy(III) sorption on MNP@Verm1.0, as evidenced by higher R^2_{adj} values and lower AIC values (Table S4). The PSO rate constants for Nd(III) and Dy(III) uptake were 5.60×10^{-4} and 6.51×10^{-4} g/μmol per minute, respectively. In addition, the estimated equilibrium q_e values were 68.1 and 47.3 μmol/g for Nd(III) and Dy(III). In contrast, for Alg@MNP@Verm1.0, the PFO model seems to better represent the kinetic behaviour, displaying higher R^2_{adj} and lower AIC values (Table S4). The PFO rate constants were 8.96×10^{-4} and 9.51×10^{-4} min^{-1}, with the estimated equilibrium $q_e$values of 95.6 and 92.2 μmol/g for Nd(III) and Dy(III), respectively.

PFO and PSO models can fit data from systems controlled by either surface reaction or diffusion.

However, they do not supply detailed insights into the underlying mass transfer mechanisms (Vareda, 2023). Nevertheless, Vareda (2023) suggests that combining these models with the Elovich equation, as well as the Weber and Morris and Boyd models, can help identify the rate-limiting step of the sorption, as these models are theoretically designed to describe kinetic data from systems limited by either chemisorption or diffusion.

When comparing the fits of the PFO and PSO models with the Elovich model (as shown in Table S4), it can be observed that although the Elovich model yields results similar to the PSO model, it does not provide the best description of the sorption kinetics in any of the systems studied.

Additionally, the plot of q_t *versus* $t^{0.5}$ exhibits two linear regions for MNP@Verm1.0 (Fig. S1(c)) and a linear segment that does not pass through the origin for Alg@MNP@Verm1.0 (Fig. S1(d)), suggesting that the sorption of REMs in both magnetic nanocomposites is not solely controlled by intraparticle diffusion. Furthermore, the Boyd plot method can be used to predict whether the rate-limiting step is intraparticle diffusion (indicated by a null y-intercept in the *Bt* against *t* plot) or film diffusion. For MNP@Verm1.0 (Fig. S1(e)) and for both Nd(III) and Dy(III), a straight line is observed, with the 95% confidence interval for the intercept including zero, implying that the sorption process is controlled by intraparticle diffusion, in contrast to the nonlinear correlation observed for Alg@MNP@Verm1.0 (Fig. S1(f)).

Since the results from the reaction- and diffusion-based models are consistent, it can be inferred that both intraparticle diffusion and sorption contribute to the overall sorption process in the MNP@Verm1.0 system. In the case of the Alg@MNP@Verm1.0 system, however, film diffusion, intraparticle diffusion, and sorption collectively influence the overall sorption process.

3.2.4 Equilibrium isotherms and sorption mechanisms

The equilibrium isotherms of Nd(III) and Dy(III) on MNP@Verm1.0 and Alg@MNP@Verm1.0 are shown in Figs. 8(a)–8(d).

All the isotherms presented in Fig. 8 exhibit a favourable L-shaped isotherm (Giles et al., 1960). This shape indicates a strong affinity between the sorbent and the sorbate at low concentrations and suggests no significant competition with the solvent occurs during sorption. However, while the isotherms for MNP@Verm1.0 clearly fall into subgroup L2, characterized by the formation of a plateau as the sorption sites approach saturation, the classification for Alg@MNP@Verm1.0 is less clear. The isotherms for Alg@MNP@Verm1.0 may correspond to subgroups L3 or L4, suggesting the possibility of a multi-step sorption process. This could involve the formation of new sorption surfaces (L3) or the formation of a second plateau (L4) as described in previous studies (Donohue and Aranovich, 1998).

Despite their similar classification, the two sorbents display distinct behaviours. MNP@Verm1.0 shows different sorption profiles for Nd(III) and Dy(III), indicating selective sorption between the two elements. In contrast, Alg@MNP@Verm1.0 exhibits no clear preference, sorbing both elements with comparable affinity.

Table S5 presents the best-fitting parameters for the two- and three- parameter isotherms evaluated, along with the quality metrics for each model's fit to equilibrium data. The inclusion of the three-parameter models did not improve the fitting compared with simpler models. Based on the quality criteria (higher R^2_{adj} and lower AIC and $S_{y,x}$ values), the Langmuir isotherm provided the best description of the experimental data for MNP@Verm1.0, while the Freundlich isotherm was the most suitable for Alg@MNP@Verm1.0.

The Langmuir isotherm best describes the saturation behaviour of MNP@Verm1.0 as concentration increases for both metals. The maximum sorption capacity (q_{mL}) and equilibrium constant (K_L) for Nd(III) and Dy(III) were 84.9 and 44.3 μmol/g, and 2.39 and 5.73 L/μmol, respectively. This model assumes monolayer adsorption on energetically homogeneous surfaces with no interactions between adsorbed species (Amrutha et al., 2023).

For Alg@MNP@Verm1.0 spheres, the Freundlich isotherm provided a satisfactory fit ($R^2_{adj} > 0.961$) for the sorption data of Nd(III) and Dy(III). The Freundlich equilibrium constants (K_F) and the heterogeneity factor (n_F) were similar, with values of 44.0 and 42.6 L/g and 2.99 and 2.89 for Nd(III) and Dy(III), respectively. These results align with the equilibrium profiles (Fig. 8(b)), where the isotherms of both metals were nearly identical. The Freundlich model suggests that the sorption of the two rare earth metals occurs on the heterogeneous surface of the sorbent (Ayawei et al., 2017).

These contrasting behaviours suggest that the Nd(III) and Dy(III) sorption on each sorbent occurs through different mechanisms.

The sorption of Dy(III) or Nd(III) on nanocomposites MNP@Verm1.0 and Alg@MNP@Verm1.0 appears to result from synergistic interactions between their individual components. Despite evidence of rare earth metals removal, the XPS survey of the MNP@Verm1.0

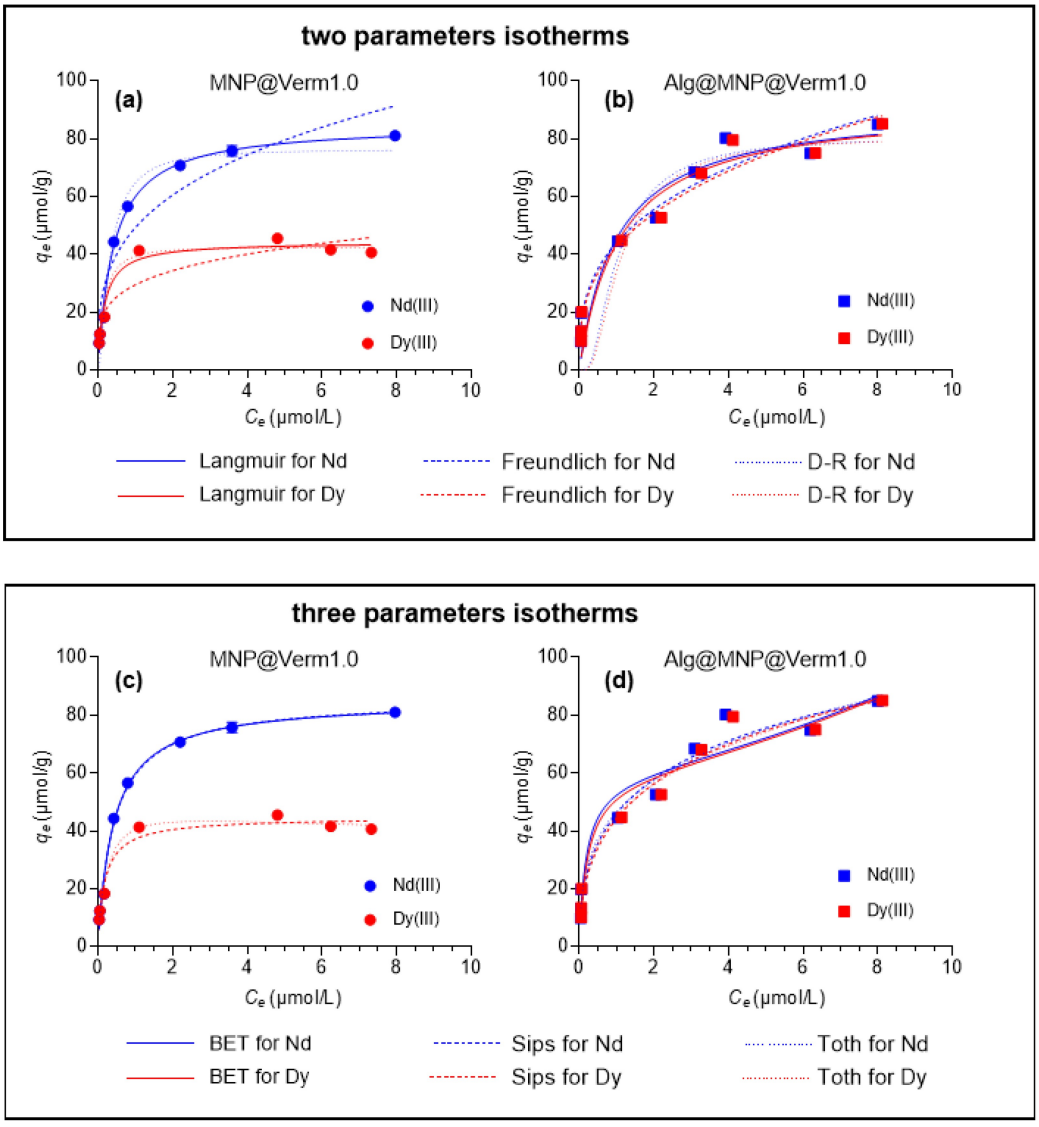

Fig. 8 Sorption isotherms of Nd(III) and Dy(III) on MNP@Verm1.0 (a and c) and Alg@MNP@Verm1.0 (b and d) nanocomposites, with the corresponding fits of the isotherm models.

and Alg@MNP@Verm1.0 after the sorption did not reveal peaks corresponding to the Dy(III) and Nd(III) (Fig. 9). That occurs because the main peaks of Dy(III) (Dy 3d5) and Nd(III) (Nd 3d5), appear in the same range of Mg 1s (~1300 eV) and O KLL (1030–980 eV), *i.e.,* there is an overlap of these peaks, which hampers the identification and determination of these REMs in the samples.

Vermiculite, a layered clay mineral, has previously demonstrated it effectively removes Dy(III) and Nd(III) through cation exchange mechanism involving Mg(II) cations (de Vargas Brião et al., 2024). The XPS survey spectra of MNP@Verm1.0 and Alg@MNP@Verm1.0, both before and after sorption, display characteristic peaks of vermiculite, including Si, Al, and Mg (Fig. 9).

However, the high-resolution XPS spectra of Mg 1s showed a distinct shift towards higher binding energies after sorption, reinforcing the hypothesis of cation exchange between the REM and the exchangeable Mg^{2+} cations in the vermiculite (Fig. 10) (de Vargas Brião et al., 2024). In addition, the high-resolution XPS spectra of Fe 2p for both samples, before and after sorption, highlighted the Fe 2p3/2 peak. Deconvolution of this peak revealed contributions from Fe(II) and Fe(III), confirming the presence of magnetite and indicating that the sorption process does not alter the integrity of the heterostructure (Fig. 10).

The deconvoluted curves of O 1s of XPS spectra of

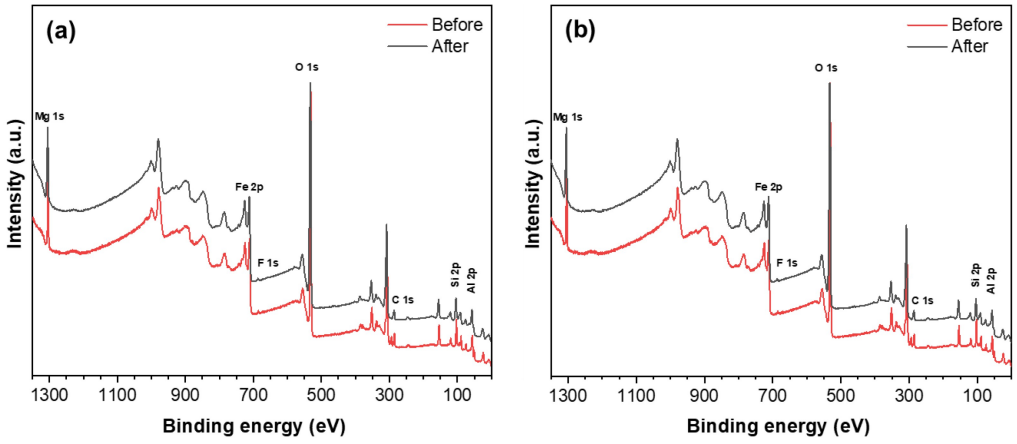

Fig. 9 Survey XPS spectrum for MNP@Verm1.0 (a) and Alg@MNP@Verm1.0 (b), before and after the sorption studies.

MNP@Verm1.0 showed peaks at 530.5, 532.3, and 535.8 eV before and 530.7, 532.7, and 535.4 eV after the sorption of Nd(III) and Dy(III). The peaks around 530 eV are related to Metal-O bonding and can be attributed to the Fe−O bond (Hou et al., 2020). This intensity and amplitude of this peak did not change after sorption, indicating the preservation of the magnetic nanoparticles in the sorbent. The signals at 532.3 and 532.7 eV revealed Si−O−Si binding (Zhang et al., 2019; Li et al., 2021). The peaks at 535.8 and 535.4 eV indicate the presence of −OH groups (Ji et al., 2019).

The high-resolution XPS spectra of O 1s of Alg@MNP@Verm1.0 before sorption exhibit three different peaks with binding energies of 536.1 eV (assigned to sodium Na KLL auger), 532.4 eV (assigned to O−H/C−O−C), and 531.1 eV (assigned to C=O), respectively (Luo et al., 2021; Hassan et al., 2022). The XPS spectra of Alg@MNP@Verm1.0 after REMs sorption could be deconvoluted into two peaks at 531.78 and 533.28 eV, indicating a shift in the C=O, C−O−C, and −OH signals, which corroborates their role in the uptake of Nd(III) and Dy(III) (Luo et al., 2021).

Based on the zeta potential results, XPS analyses, and sorption data (next section), it is possible to infer that the sorption of Nd(III) and Dy(III) on MNP@Verm1.0 may be facilitated by electrostatic interactions due to the negative charge of the sorbent, cation exchange due to the vermiculite content, and complexation with −OH groups (Zhao et al., 2024; Pinto et al, 2024). The immobilization of the nanocomposite in sodium alginate provides additional sorption sites, such as carboxyl groups, which are responsible for the complexation of REMs and the promotion of cation exchange with Na^+ (absent in the material after sorption, Table S6) (Zhang et al., 2025b).

3.2.5 Desorption studies

Desorption is an essential step for the effective recovery of high-value REMs from sorbents. It plays an important role on the viability and sustainability of the process by regenerating the sorbent's active sites while enabling the recovery of the sorbed elements.

Figure 11 illustrates the desorption efficiency achieved using six eluents categorized into three classes: inorganic salts (NH_4Cl and $MgCl_2{\cdot}6H_2O$), complexing agents (DTPA and $Na_2EDTA{\cdot}2H_2O$), and strong inorganic acids (HNO_3 and HCl). The key observation is that a higher desorption efficiency was consistently obtained for dysprosium(III) than for neodymium(III) across all eluents and sorbents tested.

NH_4Cl desorbed Nd(III) and Dy(III) with very low efficiency (< 20%), especially from the loaded alginate-immobilized nanocomposite, where the efficiency was almost zero. This insufficient performance indicates a poor exchange between NH_4^+ and the sorbed REM. On the other hand, $MgCl_2{\cdot}6H_2O$ showed desorption efficiencies of 54.9% and 76.7% for REM elution from the loaded MNP@Verm1.0. This finding suggests that the ion exchange mechanism of vermiculite plays a role in the desorption from these magnetic nanocomposites, since magnesium can exchange with the REM and regenerate the clay interlayer (de Vargas Brião et al., 2024). The same was not observed for Alg@MNP@Verm1.0, where the salt promoted much lower desorption efficiencies, indicating that the vermiculite interlayer is unavailable for ion exchange.

Strong acids performed intermediately to inorganic salts and complexing agents, with very similar desorption efficiencies. The desorption capacity achieved with nitric acid ranged from 19.7 % for Nd(III) on MNP@Verm1.0 to 63.6 % for Dy(III) on

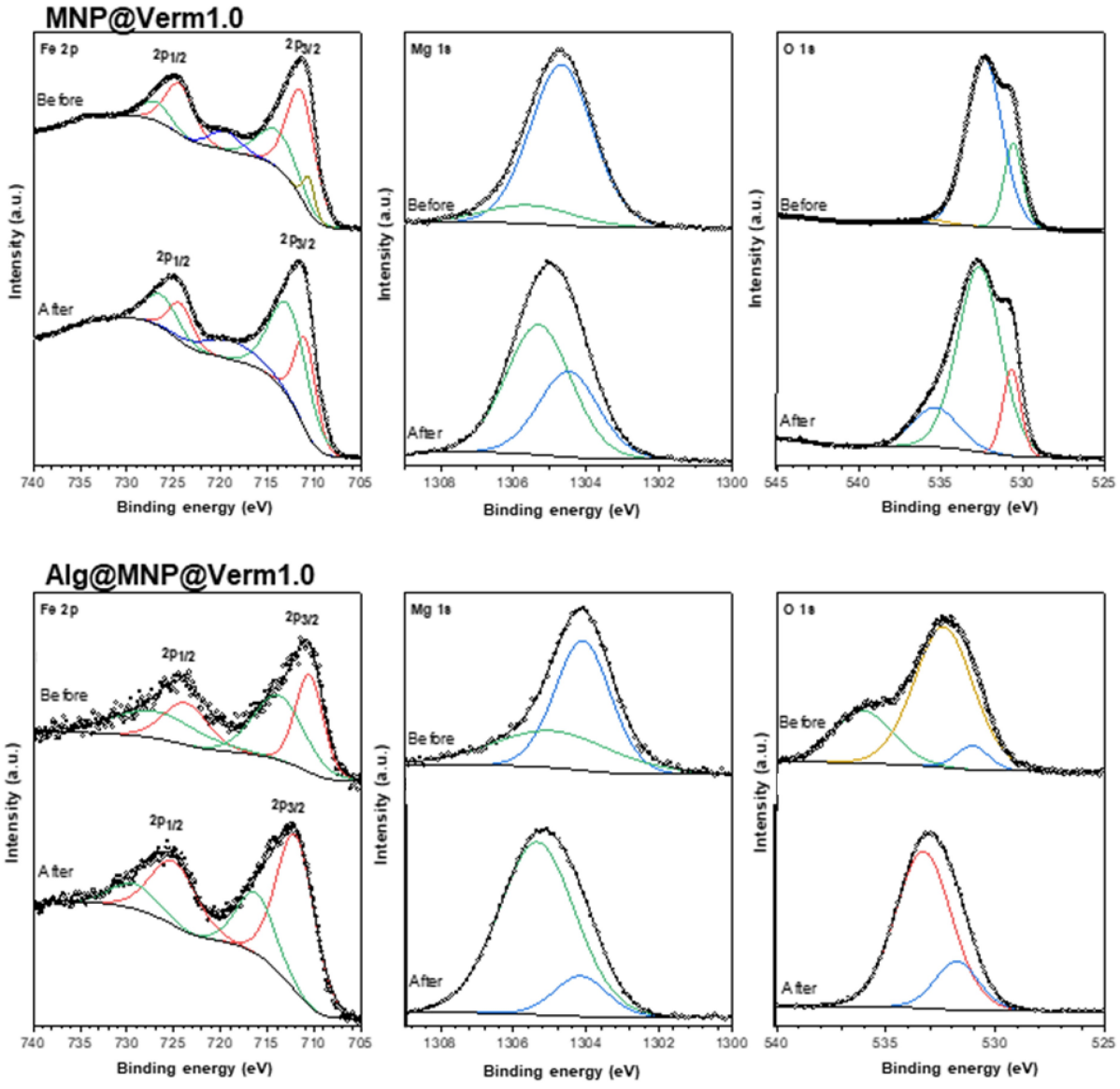

Fig. 10 High-resolution XPS spectra of Fe 2p, Mg 1s, and O 1s for MNP@Verm1.0 and Alg@MNP@Vem1.0 nanocomposites, before and after sorption.

Alg@MNP@Verm1.0. Similarly, the desorption efficiency using hydrochloric acid ranged from 18.4% to 60.1%.

Comparing the three classes of eluents, complexing agents showed the best response. DTPA performed very similarly to magnesium chloride for MNP@Verm1.0 but showed higher elution properties to recover metals from Alg@MNP@Verm1.0, with efficiencies rising to 75.5% and 94.2% for Nd(IIII) and Dy(III), respectively. Compared to DTPA, $Na_2EDTA{\cdot}2H_2O$ caused the best response for MNP@Verm1.0 and similar results for Alg@MNP@Verm1.0. The higher desorption using $Na_2EDTA{\cdot}2H_2O$, in the case of the non-alginate immobilized magnetic nanocomposite, may be related to the combined desorption mechanisms of this eluent, such as sodium exchange and REM complexation (de Vargas Brião et al., 2024).

3.3 Simulated NdFeB magnet scrap leachate

Figure 12 illustrates the sorption performance of the magnetic vermiculite-based nanocomposites, with and without alginate immobilization, for different metals from the simulated NdFeB magnet acid leachate. When exposed to the concentrated metal solution (NdFeB magnet leachate), the sorbents achieved high sorption

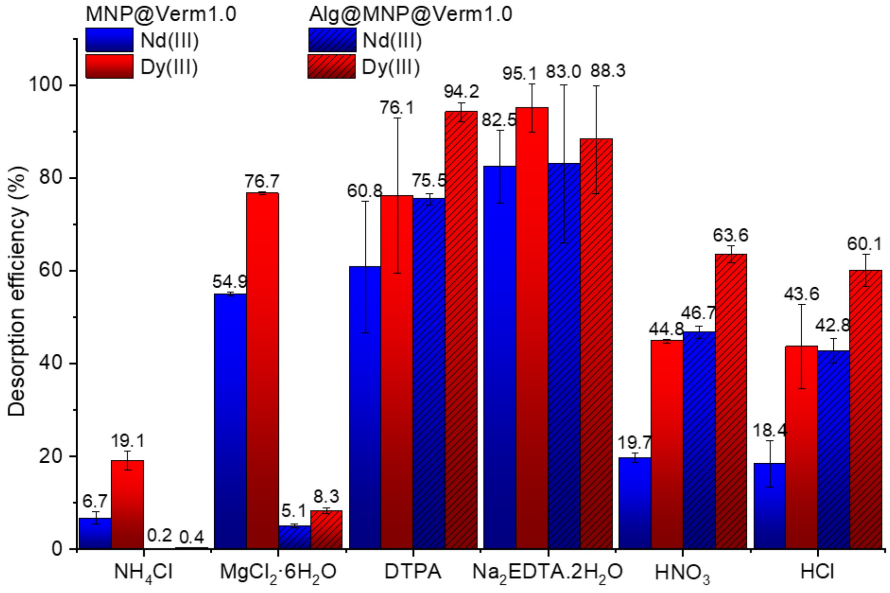

Fig. 11 Desorption performance of various eluents in the recovery of Nd(III) and Dy(III) from MNP@Verm1.0- and Alg@MNP@Verm1.0-loaded nanocomposites.

uptake values.

This improvement in sorption capacity in the simulated leachate, compared to the binary system, indicates a synergistic effect on the sorption of multiple metals. This effect is associated with the multiple sorption mechanisms involved in the system, including surface complexation, ion exchange, precipitation, and physical filling (Zhang et al., 2025a). Also, the decreasing order of sorption capacities corresponds to the decreasing order of initial concentrations of the metals in the solution (Table S6). Moreover, the difference in sorption performance between the sorbents was significantly reduced compared with the simplified binary system. Thus, the simplification of the binary system did not accurately represent what occurs during REMs sorption from leachate. The complexity of the leachate composition can lead to multiple sorption mechanisms, which requires further investigation to optimize the process and achieve scale-up objectives. Table 2 compares the performance of sorbents in retaining the main components of the NdFeB magnet acid leachate. MNP@Verm1.0 and Alg@MNP@Verm1.0 demonstrated higher sorption uptake values than the bifunctionalized silica and alginate spheres. As discussed, this superior efficiency is attributed to the abundance of oxygen-containing sorption sites on these materials.

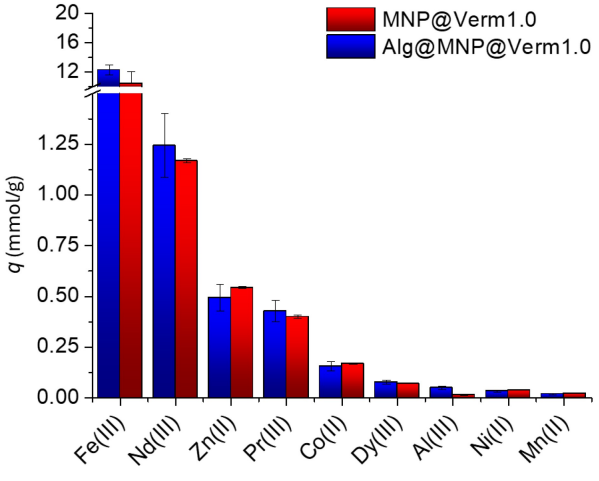

Fig. 12 Sorption uptake of MNP@Verm1.0 and Alg@MNP@Verm1.0 for multiple metals removal.

Figure 13 illustrates the regeneration performance obtained using the most efficient eluents identified in the binary solution assays, DTPA and $Na_2EDTA{\cdot}2H_2O$. These complexing agents exhibited distinct results depending on the loaded sorbent. For Alg@MNP@Verm1.0, DTPA demonstrated higher efficiency in metals desorption, whereas $Na_2EDTA{\cdot}2H_2O$ was more effective in regenerating the MNP@Verm1.0 nanocomposite. This result is consistent with the trend observed in the binary system.

Interestingly, although the loaded sorbent contained significantly more Fe(III) than Nd(III)–approximately tenfold higher–the desorbed amounts of both metals were of the same order. This means that Fe(III) is more strongly bound to the sorbents than Nd(III), as most of the loaded iron remained in the sorbent after desorption. Regardless of the eluent tested, the desorption

Table 2 Comparison of sorption efficiency for iron and REMs in the NdFeB magnet leachate

Sorbent	Removal order	Reference
Phosphorus-EDTA-funcionalized silica	Nd^{3+} (1.2 mmol/g)	Dudarko et al., 2022
	Fe^{3+} (1.1 mmol/g)	
	Dy^{3+} (0.06 mmol/g)	
	Ni^{2+} (0.02 mmol/g)	
Calcium alginate beads	Fe^{3+} (0.06 mmol/g)	Emil-Kaya et al., 2024
	Nd^{3+} (0.02 mmol/g)	
	Pr^{3+} (0.006 mmol/g)	
	Dy^{3+} (0.0006 mmol/g)	
MNP@Verm1.0	Fe^{3+} (10.5 mmol/g)	This work
	Nd^{3+} (1.17 mmol/g)	
	Pr^{3+} (0.40 mmol/g)	
	Dy^{3+} (0.07 mmol/g)	
Alg@MNP@Verm1.0	Fe^{3+} (12.3 mmol/g)	This work
	Nd^{3+} (1.24 mmol/g)	
	Pr^{3+} (0.43 mmol/g)	
	Dy^{3+} (0.08 mmol/g)	

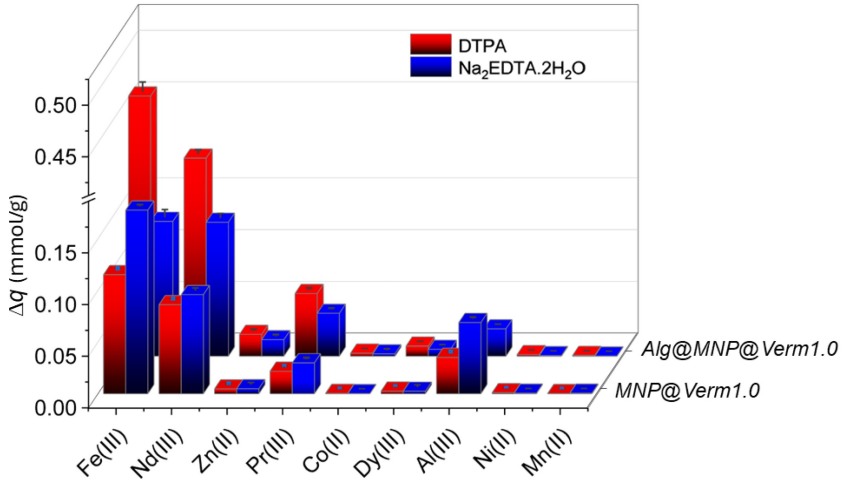

Fig. 13 Desorption efficiency of DTPA and $Na_2EDTA{\cdot}2H_2O$ for recovering REMs from the loaded sorbents.

efficiencies were generally higher for the loaded alginate-immobilized magnetic nanocomposite than for the non-immobilized counterpart, with the only exception being Al(III).

These findings confirm that immobilizing vermiculite-containing magnetic nanoparticles within alginate is an effective strategy for enhancing the desorption performance of metals-loaded MNPs. However, further studies involving successive sorption–desorption cycles are required to fully assess the long-term stability of the sorbents.

4 Conclusions

In this study, vermiculite was successfully incorporated into the synthesis of magnetite nanoparticles, and the sample with the highest vermiculite content (MNP@Verm1.0) was subsequently immobilised within alginate beads (Alg@MNP@Verm1.0). The materials were extensively characterised and evaluated for their sorption performance towards REMs (Nd(III) and Dy(III)) removal from both a binary model solution and an NdFeB magnet acid leachate.

The Alg@MNP@Verm1.0 beads exhibited magnetic

properties suitable for efficient separation under an external magnetic field. The alginate matrix introduced functional groups, such as hydroxyls and carboxyls, which improved sorption performance. Desorption studies revealed that complexing agents such as DTPA and EDTA were more effective than acids and inorganic salts in recovering the sorbed metals.

In the NdFeB magnet acid leachate, the performance of both sorbents improved with increasing metal concentrations. However, the desorption behaviour varied, with Fe(II) showing significant retention, while critical REMs such as Nd(III) exhibited substantial recovery.

These findings highlight the potential of vermiculite-modified magnetite nanoparticles, particularly those immobilized within alginate beads, for the efficient concentration and recovery of critical REMs using complexing agents. Further investigations, including successive sorption-desorption cycles, are essential to evaluate scalability and optimize the process for economic and environmental sustainability.

Conflicts of Interest The authors declare that they have no known competing financial interests or personal relationships that could have appeared to influence the work reported in this paper.

Acknowledgements The São Paulo Research Foundation (FAPESP) funded this work (Nos. 2023/09491-9 and 2017/18236-1), Coordination for the Improvement of Higher Education Personnel (CAPES) (Financial code-001), National Council for Scientific and Technological Development (CNPq) (No. 310039/2023-1). This work was also developed within the scope of the project CICECO–Aveiro Institute of Materials,UID/50011/2025&LA/P/0006/2020(DOI10.54499/LA/P/0006/2020), financed by national funds through the FCT/MCTES (PIDDAC). Thanks are also due to FCT/MCTES for the financial support to CERES (UIBD/00102/2020). Cláudia B. Lopes also thanks Fundação para a Ciência e a Tecnologia (FCT) for her research contract with reference 2021.03739.CEECIND/CP1659/CT0025 (DOI 10.54499/2021.03739.CEECIND/CP1659/CT0025). Ana Estrada acknowledges the costs of their research contracts (DL 57/2016/CP1482/CT0007; DOI: 10.54499/DL57/2016/CP1482/CT0007) resulting from the FCT hiring funded by national funds (OE), through FCT, I. P, in the scope of the framework contract foreseen in 4, 5, and 6 of article 23 of the Decree-Law 57/2016, of 29 August, changed by the law 57/2017, of 19 July. The authors kindly thank Prof. Jeffrey A. Amelse, who reviewed the manuscript for English grammar and spelling.

Electronic Supplementary Material Supplementary material is available in the online version of this article at https://dx.doi.org/10.1007/s11783-026-2167-z and is accessible for authorized users.

Funding Note Open access funding provided by FCT|FCCN (b-on).

References

Aharoni C, Tompkins F C (1970). Kinetics of adsorption and desorption and the elovich equation. Advances in Catalysis, 21: 1–49

Amorim C O, Mohseni F, Dumas R K, Amaral V S, Amaral J S (2021). A geometry-independent moment correction method for the MPMS3 SQUID-based magnetometer. Measurement Science and Technology, 32(10): 105602

Amrutha, Jeppu G, Girish C R, Prabhu B, Mayer K (2023). Multi-component adsorption isotherms: review and modeling studies. Environmental Processes, 10(2): 38

Ancira-Cortez A, Morales-Avila E, Ocampo-Garciá B E, González-Romero C, Medina L A, López-Téllez G, Cuevas-Yáñez E (2017). Preparation and characterization of a tumor-targeting dual-image system based on iron oxide nanoparticles functionalized with folic acid and rhodamine. Journal of Nanomaterials, 2017: 5184167

Artiushenko O, da Silva R F, Zaitsev V (2023). Recent advances in functional materials for rare earth recovery: a review. Sustainable Materials and Technologies, 37: e00681

Ayawei N, Ebelegi A N, Wankasi D (2017). Modelling and interpretation of adsorption isotherms. Journal of Chemistry, 2017: 3039817

Boyd G E, Adamson A W, Myers LS Jr (1947). The exchange adsorption of ions from aqueous solutions by organic zeolites. II. Kinetics. Journal of the American Chemical Society, 69(11): 2836–2848

Brewer A, Dohnalkova A, Shutthanandan V, Kovarik L, Chang E, Sawvel A M, Mason H E, Reed D, Ye C W, Hynes W F, et al. (2019). Microbe encapsulation for selective rare-earth recovery from electronic waste leachates. Environmental Science & Technology, 53(23): 13888–13897

Brunauer S, Emmett P H, Teller E (1938). Adsorption of gases in multimolecular layers. Journal of the American Chemical Society, 60(2): 309–319

Bugarčić M, Lopičić Z, Šoštarić T, Marinković A, Rusmirovic J D, Milošević D, Milivojević M (2021). Vermiculite enriched by Fe(III) oxides as a novel adsorbent for toxic metals removal. Journal of Environmental Chemical Engineering, 9(5): 106020

Callister W D Jr, Rethwisch D G (2018). Materials Science and Engineering: An Introduction. 10th ed. Hoboken: Wiley

Cardoso C E D, Almeida J C, Lopes C B, Trindade T, Vale C, Pereira E (2019). Recovery of rare earth elements by carbon-

based nanomaterials: a review. Nanomaterials, 9(6): 814

Cardoso S P, Lopes C B, Pereira E, Duarte A C, Silva C M (2013). Competitive removal of Cd^{2+} and Hg^{2+} ions from water using titanosilicate ETS-4: kinetic behaviour and selectivity. Water, Air, & Soil Pollution, 224(5): 1535

Chen L, Zhou C H, Fiore S, Tong D S, Zhang H, Li C S, Ji S F, Yu W H (2016). Functional magnetic nanoparticle/clay mineral nanocomposites: preparation, magnetism and versatile applications. Applied Clay Science, 127–128: 143–163

Ciarleglio G, Cinti F, Toto E, Santonicola M G (2023). Synthesis and characterization of alginate gel beads with embedded zeolite structures as carriers of hydrophobic Curcumin. Gels, 9(9): 714

da Costa T B, da Silva M G C, Vieira M G A (2020). Recovery of rare-earth metals from aqueous solutions by bio/adsorption using non-conventional materials: a review with recent studies and promising approaches in column applications. Journal of Rare Earths, 38(4): 339–355

da Costa T B, da Silva M G C, Vieira M G A (2021). Lanthanum biosorption using sericin/alginate particles crosslinked by poly (vinyl alcohol): kinetic, cation exchange, and desorption studies. Journal of Environmental Chemical Engineering, 9(4): 105551

da Costa T B, da Silva M G C, Vieira M G A (2022). Effective recovery of ytterbium through biosorption using crosslinked sericin-alginate beads: a complete continuous packed-bed column study. Journal of Hazardous Materials, 421: 126742

da Silva Fernandes R, de Moura M R, Glenn G M, Aouada F A (2018). Thermal, microstructural, and spectroscopic analysis of Ca^{2+} alginate/clay nanocomposite hydrogel beads. Journal of Molecular Liquids, 265: 327–336

de Vargas Brião G, de Andrade J R, da Silva M G C, Vieira M G A (2020). Removal of toxic metals from water using chitosan-based magnetic adsorbents. A review. Environmental Chemistry Letters, 18(4): 1145–1168

de Vargas Brião G, da Silva M G, Vieira M G A (2022). Adsorption potential for the concentration and recovery of rare earth metals from NdFeB magnet scrap in the hydrometallurgical route: a review in a circular economy approach. Journal of Cleaner Production, 380: 135112

de Vargas Brião G, da Silva M G C, Vieira M G A (2021). Efficient and selective adsorption of neodymium on expanded vermiculite. Industrial & Engineering Chemistry Research, 60(13): 4962–4974

de Vargas Brião G, Lopes C B, Trindade T, Silva C M, da Silva M G C, Vieira M G A (2024). NdFeB magnet scrap valorization by leaching and recovery of rare earth metals by sorption on low-cost expanded clay. Journal of Industrial and Engineering Chemistry, 131: 558–568

Delarmelinda E A, de Souza Júnior V S, Wadt P G S, Deng Y J, Campos M C C, Câmara E R G (2017). Soil-landscape relationship in a chronosequence of the middle Madeira River in southwestern Amazon, Brazil. Catena, 149: 199–208

Depraiter L, Goutte S (2023). The role and challenges of rare earths in the energy transition. Resources Policy, 86: 104137

Donohue M D, Aranovich G L (1998). Classification of Gibbs adsorption isotherms. Advances in Colloid and Interface Science, 76–77: 137–152

Dubinin M M, Radushkevich L V (1947). Equation of the characteristic curve of activated charcoal proceedings of the academy of sciences. Physical Chemistry Section USSR, 55: 331–333

Dubus J, Leonhardt N, Latrille C (2023). Multi-cation exchanges involved in cesium and potassium sorption mechanisms on vermiculite and micaceous structures. Environmental Science and Pollution Research, 30(1): 1579–1594

Dudarko O, Kobylinska N, Kessler V, Seisenbaeva G (2022). Recovery of rare earth elements from NdFeB magnet by mono- and bifunctional mesoporous silica: waste recycling strategies and perspectives. Hydrometallurgy, 210: 105855

Emil-Kaya E, Uysal E, Dikmetas D N, Karbancioğlu-Güler F, Gürmen S, Friedrich B (2024). Development of a near-zero-waste valorization concept for waste NdFeB magnets: production of antimicrobial Fe alginate beads via adsorption and recovery of high-purity rare-earth elements. ACS Omega, 9(6): 6442–6454

Feng J P, Liu M, Fu L Z, Zhang K, Xie Z H, Shi D W, Ma X (2020). Enhancement and mechanism of vermiculite thermal expansion modified by sodium ions. RSC Advances, 10(13): 7635–7642

Filho W L, Kotter R, Özuyar P G, Abubakar I R, Eustachio J H P P, Matandirotya N R (2023). Understanding rare earth elements as critical raw materials. Sustainability, 15(3): 1919

Freundlich H M F (1906). Over the adsorption in solution. The Journal of Physical Chemistry, 57: 385–471

Gautam B, Nabat Al-Ajrash S M, Hasan M J, Saini A, Watzman S J, Ureña-Benavides E, Vasquez-Guardado E S (2024). Experimental thermal conductivity studies of agar-based aqueous suspensions with lignin magnetic nanocomposites. Magnetochemistry, 10(2): 12

Ghasemi A (2022). Ferrite characterization techniques. In: Ghasemi A, ed. Magnetic Ferrites and Related Nanocomposites. Amsterdam: Elsevier, 49–124

Giles C H, MacEwan T H, Nakhwa S N, Smith D (1960). Studies in adsorption. Part XI. A system of classification of solution adsorption isotherms, and its use in diagnosis of adsorption mechanisms and in measurement of specific surface areas of solids. Journal of the Chemical Society (Resumed), 3973–3993

González-Martínez E, Pérez A G, González-Martínez D A, Águila C R D, Urbina E C, Ramírez D U, Yee-Madeira H (2021). Chitosan-coated magnetic nanoparticles: exploring their potentialities for DNA and Cu(II) recovery. Inorganic and Nano-Metal Chemistry, 51(8): 1098–1107

Hassan M, Naidu R, Du J H, Qi F J, Ahsan M A, Liu Y J (2022). Magnetic responsive mesoporous alginate/*β*-cyclodextrin polymer beads enhance selectivity and adsorption of heavy metal ions. International Journal of Biological Macromolecules, 207: 826–840

Hisada M, Kawase Y (2018). Recovery of rare-earth metal neodymium from aqueous solutions by poly-γ-glutamic acid and

its sodium salt as biosorbents: effects of solution pH on neodymium recovery mechanisms. Journal of Rare Earths, 36(5): 528–536

Ho Y S, McKay G (1998). A comparison of chemisorption kinetic models applied to pollutant removal on various sorbents. Process Safety and Environmental Protection, 76(4): 332–340

Ho Y S, McKay G (1999). Pseudo-second order model for sorption processes. Process Biochemistry, 34(5): 451–465

Hou L, Liang Q B, Wang F (2020). Mechanisms that control the adsorption–desorption behavior of phosphate on magnetite nanoparticles: the role of particle size and surface chemistry characteristics. RSC Advances, 10(4): 2378–2388

Hu Q L, Zhang Z Y (2019). Application of Dubinin–Radushkevich isotherm model at the solid/solution interface: a theoretical analysis. Journal of Molecular Liquids, 277: 646–648

Ji Y L, Zhang H M, Zhang C F, Quan Z Y, Huang M, Wang L L (2019). Fluorescent and mechanical properties of silicon quantum dots modified sodium alginate-carboxymethylcellulose sodium nanocomposite bio-polymer films. Polymers, 11(9): 1476

Jung Y, Lee Y, Yoon S J, Choi J W (2024). Synergistic effect of core/shell-structured composite fibers: efficient recovery of rare-earth elements from spent NdFeB permanent magnets. Advanced Fiber Materials, 6(6): 1729–1745

Jyothi R K, Thenepalli T, Ahn J W, Parhi P K, Chung K W, Lee J Y (2020). Review of rare earth elements recovery from secondary resources for clean energy technologies: grand opportunities to create wealth from waste. Journal of Cleaner Production, 267: 122048

Kegl T, Košak A, Lobnik A, Novak Z, Kralj A K, Ban I (2020). Adsorption of rare earth metals from wastewater by nanomaterials: a review. Journal of Hazardous Materials, 386: 121632

Kloster G A, Muraca D, Moscoso Londoño O, Pirota K R, Mosiewicki M A, Marcovich N E (2020). Alginate based nanocomposites with magnetic properties. Composites Part A: Applied Science and Manufacturing, 135: 105936

Kragović M, Daković A, Marković M, Petković A (2016). Kinetic of thermal degradation of alginate-zeolite composites. Zastita Materijala, 57(4): 559–564

Kucuker M A, Wieczorek N, Kuchta K, Copty N K (2017). Biosorption of neodymium on *Chlorella vulgaris* in aqueous solution obtained from hard disk drive magnets. PLoS One, 12(4): e0175255

Lagergren S (1898). About the theory of so-called adsorption of soluble substances. Kungliga Svenska Vetenskapsakademiens. Handlingar, Band, 24(4): 1–39

Langmuir I (1918). The adsorption of gases on plane surfaces of glass, mica and platinum. Journal of the American Chemical Society, 40(9): 1361–1403

Li B, Yuan X Q, Li B T, Wang X J (2021). Ceria-modified nickel supported on porous silica as highly active and stable catalyst for dry reforming of methane. Fuel, 301: 121027

Li J R, Gong A J, Li F K, Qiu L N, Zhang W W, Gao G, Liu Y, Li J D (2018). Synthesis and characterization of magnetic mesoporous Fe_3O_4@mSiO_2–DODGA nanoparticles for adsorption of 16 rare earth elements. RSC Advances, 8(68): 39149–39161

Liang Y, Lu W L (2020). Gamma-irradiation synthesis of Fe_3O_4/rGO nanocomposites as lithium-ion battery anodes. Journal of Materials Science: Materials in Electronics, 31(19): 17075–17083

Lu W (2012). Self-assembly of nanostructures. In: Bhushan B, ed. Encyclopedia of Nanotechnology. Dordrecht: Springer, 2371–2382

Luo H Y, Liu Y, Lu H X, Fang Q, Rong H W (2021). Efficient adsorption of tetracycline from aqueous solutions by modified alginate beads after the removal of Cu(II) ions. ACS Omega, 6(9): 6240–6251

Macedo V M, Pereira N, Tubio C R, Martins P, Costa C M, Lanceros-Mendez S (2022). Carrageenan based printable magnetic nanocomposites for actuator applications. Composites Science and Technology, 224: 109485

Malla P B (1978). Vermiculite. In: Fairbridge R W, Bourgeois, eds. Encyclopedia of Sedimentology. Berlin Heidelberg: Springer, 1265–1269

Marangoni Júnior L, Rodrigues P R, da Silva R G, Vieira R P, Alves R M V (2021). Sustainable packaging films composed of sodium alginate and hydrolyzed collagen: preparation and characterization. Food and Bioprocess Technology, 14(12): 2336–2346

Molina-Calderón L, Basualto-Flores C, Paredes-García V, Venegas-Yazigi D (2022). Advances of magnetic nanohydrometallurgy using superparamagnetic nanomaterials as rare earth ions adsorbents: a grand opportunity for sustainable rare earth recovery. Separation and Purification Technology, 299: 121708

Monazam E R, Breault R W, Siriwardane R (2014). Kinetics of magnetite (Fe_3O_4) oxidation to hematite (Fe_2O_3) in air for chemical looping combustion. Industrial & Engineering Chemistry Research, 53(34): 13320–13328

Pawar R R, Lalhmunsiama, Ingole P G, Lee S M (2020). Use of activated bentonite-alginate composite beads for efficient removal of toxic Cu^{2+} and Pb^{2+} ions from aquatic environment. International Journal of Biological Macromolecules, 164: 3145–3154

Pinto J, Fernandes R, Tavares D, Henriques B, Trindade T, Pereira E (2024). Removal of Rare Earth Elements from complex mixtures by using manganese ferrite nanoparticles: optimization through surface response methodology. Journal of Environmental Management, 368: 122211

Rahman S S U, Qureshi M T, Sultana K, Rehman W, Khan M Y, Asif M H, Farooq M, Sultana N (2017). Single step growth of iron oxide nanoparticles and their use as glucose biosensor. Results in Physics, 7: 4451–4456

Rahmatika A M, Toyoda Y, Nguyen T T, Goi Y, Kitamura T, Morita Y, Kume K, Ogi T (2020). Cellulose nanofiber and magnetic nanoparticles as building blocks constructing biomass-based porous structured particles and their protein adsorption

performance. ACS Sustainable Chemistry & Engineering, 8(50): 18686–18695

Rakotomalala Robinson M, Abdelmoula M, Mallet M, Coustel R (2023). The role of starch in nano-magnetite formation: a spectrometric and structural investigation. Materials Chemistry and Physics, 297: 127285

Schwertmann U, Cornell R M (2000). Iron Oxides in the Laboratory: Preparation and Characterization. Weinheim: Wiley-VCH

Simonin J P (2016). On the comparison of pseudo-first order and pseudo-second order rate laws in the modeling of adsorption kinetics. Chemical Engineering Journal, 300: 254–263

Sips R (1948). On the structure of a catalyst surface. The Journal of Chemical Physics, 16(5): 490–495

Srivastava S, Bajpai A, Musthaq S M, Biswas K (2024). Recovery of rare earth elements (Nd, Dy) from discarded hard disk magnets using EDTA functionalised chitosan. RSC Sustainability, 2(4): 1088–1100

Tan K L, Hameed B H (2017). Insight into the adsorption kinetics models for the removal of contaminants from aqueous solutions. Journal of the Taiwan Institute of Chemical Engineers, 74: 25–48

Tóth J (1995). Uniform interpretation of gas/solid adsorption. Advances in Colloid and Interface Science, 55: 1–239

Tóth J (1997). Some consequences of the application of incorrect gas/solid adsorption isotherm equations. Journal of Colloid and Interface Science, 185(1): 228–235

Valášková M, Kočí K, Madejová J, Matějová L, Pavlovský J, Barrocas B T, Klemencová K (2022). α-Fe_2O_3 nanoparticles/iron-containing vermiculite composites: structural, textural, optical and photocatalytic properties. Minerals, 12(5): 607

Vareda J P (2023). On validity, physical meaning, mechanism insights and regression of adsorption kinetic models. Journal of Molecular Liquids, 376: 121416

Viegas R M C, Campinas M, Costa H, Rosa M J (2014). How do the HSDM and Boyd's model compare for estimating intraparticle diffusion coefficients in adsorption processes. Adsorption, 20(5): 737–746

Vuppaladadiyam S S V, Thomas B S, Kundu C, Vuppaladadiyam A K, Duan H B, Bhattacharya S (2024). Can e-waste recycling provide a solution to the scarcity of rare earth metals? An overview of e-waste recycling methods. Science of the Total Environment, 924: 171453

Wang J L, Guo X (2020). Adsorption kinetic models: physical meanings, applications, and solving methods. Journal of Hazardous Materials, 390: 122156

Weber W J Jr, Morris J C (1963). Kinetics of adsorption on carbon from solution. Journal of the Sanitary Engineering Division, 89(2): 31–59

Wu F C, Tseng R L, Juang R S (2009). Characteristics of Elovich equation used for the analysis of adsorption kinetics in dye-chitosan systems. Chemical Engineering Journal, 150(2−3): 366–373

Xiang H, Yang Z, Liu X, Lu F, Zhao F, Chai L (2025). Advancements in functional adsorbents for sustainable recovery of rare earth elements from wastewater: a comprehensive review of performance, mechanisms, and applications. Advances in Colloid and Interface Science, 338: 103403

Ye Q H, Jin X Y, Zhu B T, Gao H F, Wei N (2023). Lanmodulin-functionalized magnetic nanoparticles as a highly selective biosorbent for recovery of rare earth elements. Environmental Science & Technology, 57(10): 4276–4285

Zhang D, Wu B, Wang T T, Yılmaz M, Sharma G, Kumar A, Shi H (2025a). Multi-mechanism synergistic adsorption of lead and cadmium in water by structure-functionally adapted modified biochar: a review. Desalination and Water Treatment, 322: 101156

Zhang Y, Zhu L L, Chen L G, Liu L Q, Ye G T (2019). Influence of magnesia on demoulding strength of colloidal silica-bonded castables. Reviews on Advanced Materials Science, 58(1): 32–37

Zhang Y Y, Cai W L, Chen Z L (2025b). Sodium alginate/polyvinyl alcohol for the recovery of rare earth elements from mining wastewater: mechanism and properties. Separation and Purification Technology, 354: 128735

Zhao C X, Wang J, Yang B J, Liu Y, Qiu G Z (2024). Selective separation of rare earth ions from mine wastewater using synthetic hematite nanoparticles from natural pyrite. Minerals, 14(5): 464